Closing the Cell-to-Module Efficiency Gap: A Fully Laser Scribed Perovskite Minimodule With 16% Steady-State Aperture Area Efficiency

Arnaud Walter, Soo-Jin Moon, Brett A. Kamino, Linus Löfgren, Davide Sacchetto, Fabio Matteocci, Babak Taheri, Julien Bailat, Aldo Di Carlo, Christophe Ballif, and Sylvain Nicolay

***Abstract*—Organic–inorganic halide perovskite solar cells show increasing power conversion efficiencies, approaching the values of silicon-based devices. To date, however, most of the reported record efficiencies for perovskite solar devices are obtained on single cells with active areas significantly below 1 cm^2. Hence, demonstrating highly efficient devices with an upscaled active area is one of the key challenges faced by this technology. Here, we demonstrate the successful use of thin-film laser patterning techniques to produce 14 cm^2 modules with steady-state aperture area efficiencies as high as 16% and a geometrical fill factor of 92%.**

***Index Terms*—Laser scribing, monolithic modules, organic–inorganic hybrid materials, perovskite, series interconnection, solar cells.**

I. Introduction

In RECENT years, a new class of thin-film PV absorber—the organic–inorganic halide perovskite (PK)—has gained significant interest, leading to an unprecedented rise in device efficiency [1]. Indeed, PK solar cells hold the promise of high efficiency (>20% certified efficiency [2]) and low processing costs [3] while offering the flexibility of a thin-film technology. However, despite the great efforts put into the race to reach record efficiencies, most of the reported results so far were obtained on devices with a scale significantly smaller than the symbolic mark of 1 cm^2 [4], [5]. Therefore, there is an urgent need for demonstrating the potential to upscale this promising technology as an essential step toward the proof of its industrial viability.

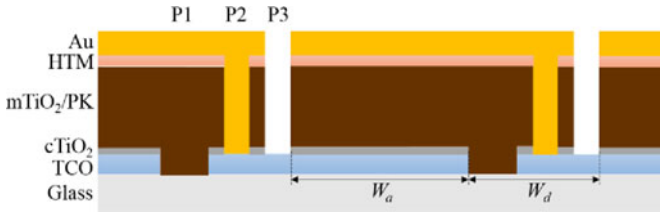

Fig. 1. Schematic of the interconnection showing the P1–P2–P3 lines for a scaffold module.

The first reported monolithic PK-based module showed an efficiency of 5.1% for an aperture area of 25 cm^2 (active area 16.8 cm^2) [6]. The same group later demonstrated the use of laser patterning to define some of the interconnection lines. Together with an improved deposition scheme involving the blade coating of the PbI_2 precursor, this led to an improved module efficiency of 10.4% on 10.1 cm^2 and 4.3% on 100 cm^2. However, the fraction of dead area was still as high as 27% of the total aperture area [7]. The use of a *fully* laser-patterned interconnection, widely applied in other thin-film PV technologies, enables a greatly reduced fraction of dead area [8]. Moon *et al.* successfully demonstrated such fully laser-patterned PK modules, reducing the fraction of dead area to 16%, and leading to an aperture area efficiency of 5.52% on 6 cm^2 [9]. The same contribution identified the impact of the dead area on the relative power loss of the module. Relying on a similar laser patterning, Qiu *et al.* [10] have very recently shown an outstanding efficiency of 16.4% on a small 4 cm^2 aperture area module thanks to an optimized perovskite composition. Others have developed improved deposition techniques suitable for large area coating, such as chemical vapor deposition [11] or infiltration of a mesoporous carbon electrode with the perovskite [12]. However, these rely on screen-printing or photolithography to realize the interconnection, still leading to large inactive area losses.

Practically, serial interconnection relies on three successive patterning steps, called P1, P2, and P3 [13]. As depicted in Fig. 1, the P1 pattern isolates the front transparent conductive oxide (TCO) of successive segments. By removing the active layer down to the front TCO, the P2 line enables contact between the subsequent back metallization and the front TCO. Finally, the P3 pattern completes the interconnection by separating two

Manuscript received June 9, 2017; revised September 22, 2017; accepted October 17, 2017. Date of publication November 3, 2017; date of current version December 20, 2017. The project comprising this work is evaluated by the Swiss National Science Foundation and supported in part by Nano-Tera.ch and in part by the NRP 70 "Energy Turnaround" Program with financing from the Swiss National Science Foundation and the Swiss Federal Office of Energy, under Grant SI/501072-01. This work was supported by the European Union's Horizon 2020 research and innovation program under Grant 653296 (CHEOPS). *(Corresponding author: Arnaud Walter.)*

A. Walter, S.-J. Moon, B. A. Kamino, L. Löfgren, D. Sacchetto, J. Bailat, C. Ballif, and S. Nicolay are with the CSEM PV-Center, Neuchâtel 2002, Switzerland (e-mail: arnaud.walter@csem.ch; soo-jin.moon@csem.ch; brett.kamino@csem.ch; linus.loefgren@csem.ch; davide.sacchetto@csem.ch; julien.bailat@csem.ch; christophe.ballif@csem.ch; sylvain.nicolay@csem.cha).

F. Matteocci, B. Taheri, and A. Di Carlo are with the Centre for Hybrid and Organic Solar Energy, University of Rome "Tor Vergata", Rome 00133, Italy (e-mail: fabio.matteocci@uniroma2.it; babak.taheri@uniroma2.it; aldo.dicarlo@uniroma2.it).

This paper has supplementary downloadable material available at http://ieeexplore.ieee.org.

Color versions of one or more of the figures in this paper are available online at http://ieeexplore.ieee.org.

Digital Object Identifier 10.1109/JPHOTOV.2017.2765082

successive segments and isolating their back contact. The area between the P1 and the P3 lines is, thus, no longer an active part of the cell area. This dead area is characterized by its width W_d (as opposed to the active area width W_a). As previously explained, a trade-off has to be found between the limitation of W_d, leading to current losses, and W_a, leading to resistive losses in the TCO [9]. As such, being able to optimize the dead area is crucial in order to limit the loss of performance when upscaling from a small cell to a module [14].

The present work reports on the use of laser scribing to pattern optimized P1, P2, and P3 interconnection lines on PK modules. We demonstrate that this technique is well-suited to scribe scaffold-based modules. Specifically, we show how laser scribing can be applied to modules including a compact TiO_2 blocking layer and a mesoporous scaffold. Moreover, we show that the use of optimized laser parameters allows for the controlled patterning of the metallic back electrode. Finally, by combining the reduced dead area enabled by laser patterning with improved deposition processes by spin-coating, modules with record efficiencies as high as 16.0% on 14 cm^2 aperture area were achieved, thus approaching the performance of other commercial thin-film technologies [2].

II. Experimental Details

A. Solar Cells and Modules Fabrication

Fluorine doped tin oxide (FTO)/glass (Solaronix TCO22-7/LI) substrates were coated with 20 nm TiO_{2-x} deposited by RF sputtering to form the front electrode/hole blocking layer stack. A UV laser (Newport BLS, 355 nm, nanosecond pulse) was used to scribe through the glass the P1 isolation line to define the module segments (seven segments/module). A double P1 line is used to ensure proper isolation of each segment. The module was subsequently spin-coated with a 150 nm thick mesoporous TiO_2 layer and annealed at 500 °C.

The $CH_3NH_3PbI_3$ (MALI) perovskite precursor solution and deposition were adapted from Ahn *et al.* [15]. Namely, a stoichiometric amount of MAI, PbI_2, and dimethyl sulfoxide (DMSO) (1:1:1 mol%) was dissolved in N, N-dimethylformamide (DMF). During the spin-coating of the precursor solution, diethyl ether (DEE) was poured onto the substrate to aid in film formation by precipitating the perovskite precursor. Upon subsequent drying and annealing at 100 °C for 10 min, the film crystallized to form the desired perovskite layer. The solution-processed $Cs_{0.05}(MA_{0.17}FA_{0.83})_{0.95}Pb(I_{0.83}Br_{0.17})_3$ (so-called triple cation PK, hereafter CsFAMA) was deposited according to Saliba *et al.* [16]. The perovskite film was spun from a precursor solution of DMF/DMSO (4:1 v:v). Chlorobenzene was used this time as the antisolvent and dripped on the substrate before the end of the spin-coating step. Substrates were subsequently annealed.

The hole transport material (regardless of the type of module) was spiro-OMeTAD blended with tBP and Li:TFSI, deposited by spin coating under N_2 atmosphere.

All modules were then P2-scribed from the glass side using a 532 nm laser (Newport Explorer). Finally, an Au (100 nm) top contact was thermally evaporated followed by a final P3 scribe process using a 532 nm laser from the layer side. The P2 and P3 lines were doubled to enable an effective contact between the front TCO and the Au contact, and a good isolation of the segments, respectively. More details about the laser parameters can be found in the Supplementary information.

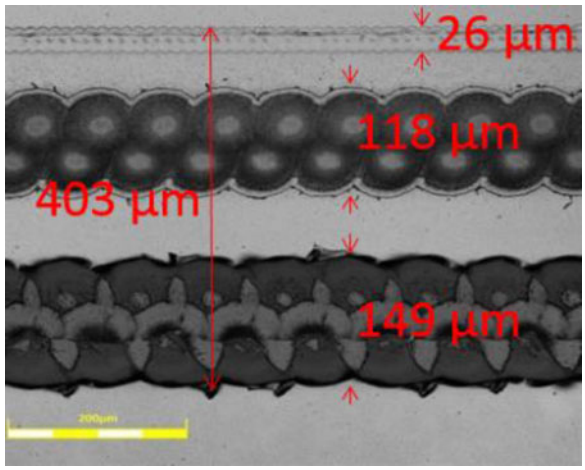

Fig. 2. Confocal microscope image of a module's P1–P2–P3 interconnection lines (from top to bottom).

B. Characterization

Current–voltage measurements were carried out on a two-lamp (halogen and xenon) class AAA WACOM sun simulator with an AM1.5 g irradiance spectrum at 1000 W/ m^2. Each device is characterized both in forward (from J_{SC} to V_{OC}) and reverse (from V_{OC} to J_{SC}) direction. A maximum power point (MPP) tracking algorithm allows for the extraction of the steady-state power output. An electrical fan provides an active cooling to the measurement chuck, preventing the substrate from heating during the prolonged measurement. External quantum efficiency (EQE) spectra were recorded on a custom-made spectral response setup consisting of a xenon lamp, a grating monochromator, and two lock-in amplifiers, with a chopped light beam at a frequency of 10 Hz. The beam size is 2 mm^2. No additional bias light was used.

To obtain light-beam-induced current (LBIC) maps, an inverted microscope (Leica DMI 5000) coupled with a monochromator (Cornerstone 130) was used to get a 530 nm ($\pm$2 nm) light beam from a 200 W xenon lamp. A long working objective focused the beam to a 50 $\times$ 50 μm spot. An x–y-motorized stage enabled us to scan the modules by steps of 500 μm. By means of a chopper, a photodiode, and lock-in amplifiers, the current of the device could be precisely measured.

Laser scribing lines are imaged by mean of a confocal microscope (Olympus Lext OLS4000).

III. Results and Discussion

An important requirement for realizing high-performance interconnected thin-film modules is minimizing the power losses from both the dead area caused by the laser scribes and the resistive losses from the front TCO. To this end, we have optimized our laser interconnection process to achieve this aim. Fig. 2 shows a confocal microscope image of a fully laser-patterned

interconnection. For the P1 line, a UV laser was used, resulting in a very narrow P1 line (<30 μm). The optimized line is the result of two overlapping scribing passes to ensure adequate isolation of the TCO front contact (∼15 μm each, 15 μm apart). The P2 and P3 lines, scribed by a green laser, are wider (∼120 and 150 μm, respectively). In the case of the P2 scribe, this width is dictated by the need for a complete removal of the underlying mesoporous TiO_2 scaffold to achieve minimal contact resistance between the back metallization and the front TCO. When the pulse energy is too low, the P2 scribing process leaves part of the TiO_2 scaffold behind (see Fig. S1), which strongly affects the fill factor (FF) and current extraction. The optimized P2 scribe consists of two lines of 40 μm in width (40 μm apart). For the P3 line (50 μm per line, 50 μm overlap), we found that one challenge was avoiding delamination of the Au back contact from the scribing process (see Fig. S2). The laser energy chosen is strongly absorbed by the perovskite layer when illuminated through the substrate side. Therefore, we hypothesize that an explosion cone is formed that tears apart the gold layer resulting in significant delamination. This is consistent with an ablation/lift-off type of perovskite removal by laser, as observed elsewhere [17]. This has two undesired side effects: first, a possible resettling of gold flakes inside the scribe that can short two consecutive segments, and second, a current loss at the delaminated areas. In order to minimize this, we have scribed the P3 line directly from the metal side, which considerably reduces the delamination as compared to our previous work [9]. We speculate that the green laser pulse is primarily absorbed within the metal layer providing a clean cut of the said layer. This is supported by Fig. S3. Further improvements could be achieved by replacing the gold by another metal electrode with a better adhesion to the underlying stack. From this optimization of the laser scribe lines, W_d was successfully reduced to ∼400 μm for a total segment width ($W_d + W_a$) of 5 mm, which represents an 8% dead area fraction. Details on the power losses analysis can be found in the Supplementary information.

Beyond minimized power losses, a crucial constraint for upscaling perovskite solar cells to modules is the uniformity of the absorber layer. Indeed, lab-scale single cells are typically processed on substrates with a size of a few square centimeters. On such a scale, very uniform layers can be obtained by spin coating, leading, in our case, to reference cells with a steady-state efficiency >17% on 1 cm^2 active area. However, it has proven to be challenging to maintain a good uniformity of the PK layer on larger scales (substrate size: 5 × 5 cm^2). Therefore, two different PK compositions involving the use of different antisolvents (see Section II) have been investigated.

The first approach used to deposit the MALI perovskite structure onto a mesoporous substrate led to a 7-interconnected segment module with an initial aperture area efficiency of 14.4% (steady-state during MPP tracking at 14.1%), as shown in Fig. 3. The aperture area of the module is 14 cm^2. This module shows a high V_{OC} of ∼7.4 V, corresponding to ∼1.06 V/seg. This value is close to our best 1 cm^2 MALI reference cell measured at ∼1.1 V V_{OC}. Nevertheless, there is a mismatch between V_{OC} of the module and that of the single cell that we can link to the slightly lower quality of the PK layer over the full module area,

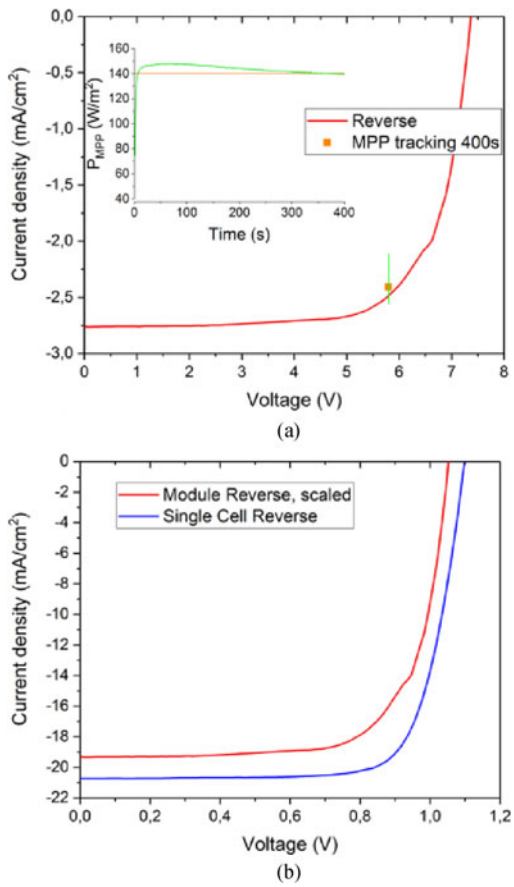

Fig. 3. MALI module (a). The inset shows the MPP tracking. The steady-state MPP settles on the reverse scan. (b) The comparison between a single cell and a module (scaled).

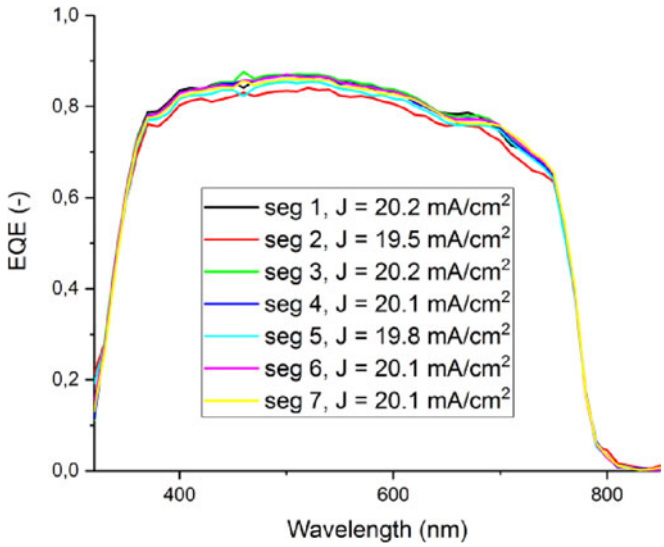

Fig. 4. External quantum efficiency of an MALI module, segment by segment.

as discussed later. Moreover, when scaled to a single segment, the short-circuit current density is 19.3 mA/ cm^2, which is lower than that of the reference cell by approximately 1.2 mA/ cm^2. This loss in current can be ascribed to the dead area induced by the interconnection. This is supported by the fact that the integrated current from the EQE for each segment (see Fig. 4)

TABLE I
SUMMARY OF *IV* PARAMETERS

		Aperture area [cm^2]	Scan direction	V_{OC} [mV]	J_{SC} [mA/cm^2]	FF [%]	Eff. [%]	Steady-state MPP Eff. [%]
MALI	Module	14	Reverse	7370	2.76	70.8	14.4	14.1
			Forward	7368	2.75	63.6	13.3	
	Ref. cell	1.04	Reverse	1099	20.7	75.6	17.2	17.3
			Forward	1108	20.5	68.8	15.7	
CsFAMA	Module	14	Reverse	8061	2.74	75.0	16.6	16.0
			Forward	7755	2.73	62.0	13.1	
	Ref. cell	1.04	Reverse	1165	20.5	72.0	17.2	16.7
			Forward	1152	20.6	70.0	16.6	

Summary of *IV* parameters for different compositions of perovskite. The table presents results of modules as well as the corresponding small area single cells references.

stays close to that of the reference cell, showing the relatively good quality of the absorber film. Eventually, it is also seen that the steady-state efficiency tracked at MPP is lower than the one measured in the reverse *IV* scan, which could be attributed to prolonged light soaking and increased temperature of the module during successive measurements [18].

The triple-cation perovskite (CsFAMA) formulation has been shown to improve the stability and reproducibility of PK (small area) single cells while having the potential for higher efficiency [16]. To explore any potential benefits of this formulation, we applied it to a similar mesoporous module as mentioned above. Thanks to a careful control over the spin coating and annealing parameters, very uniform, pinhole-free films could be obtained, as confirmed by LBIC mapping (see Fig. 6). Thus, while the 1 cm^2 reference cells exhibited steady-state efficiencies as high as 16.7%, the 7-segments module showed a remarkable 16.0% aperture area efficiency (steady-state). Such a module, while having a similar current as the MALI module, possesses a higher open-circuit voltage >8 V owing to the slightly higher band gap of the bromine-containing perovskite (see Fig. 5). Table I summarizes the cell and module results for the different PK systems. It is noteworthy that the FF of the CsFAMA module is higher than its cell counterpart. This is a direct consequence of a well-designed module and of the small dead area width. Photogenerated charges extracted in the front TCO have only to travel to the next P2 line to reach the metallic contact and will have minimal electronic resistance from traveling through the TCO. In comparison, the design of the single cells is such that the contact to the front TCO is further apart from the active area, increasing series resistance and reducing FF.

In order to assess the uniformity of the PK/spiro-OMeTAD coating, LBIC measurement was performed. By locally illuminating the module at the wavelength of the maximum of absorption of the PK, one can obtain a precise spatial distribution of the current generation across the whole module [19]. The LBIC map, shown in Fig. 6, is very uniform over the full extent of the segments, showing no edge effect due to the spin-coating process. In comparison, the MALI module exhibits significant discrepancies in the current distribution, with a pronounced difference between the central area and the edges. This is ascribed to the different processes used to coat both types of

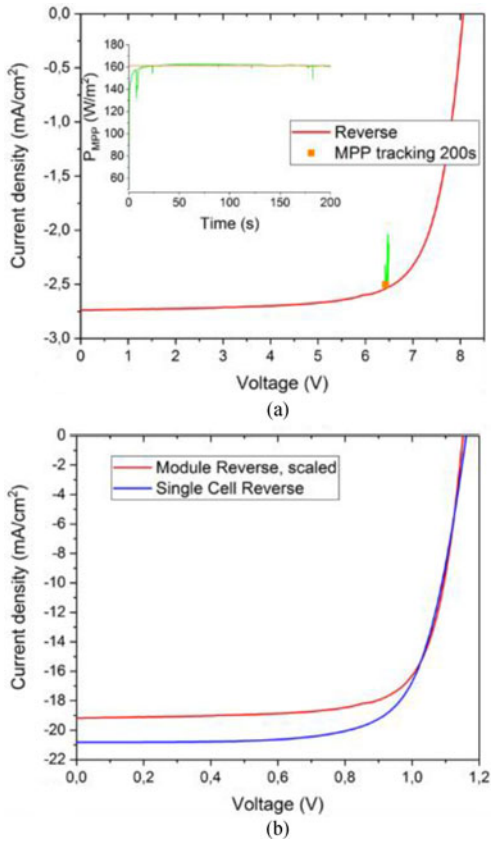

Fig. 5. CsFAMA module (a). The inset shows the MPP tracking. The steady-state MPP settles on the reverse scan. (b) The comparison between a single cell and a module (scaled).

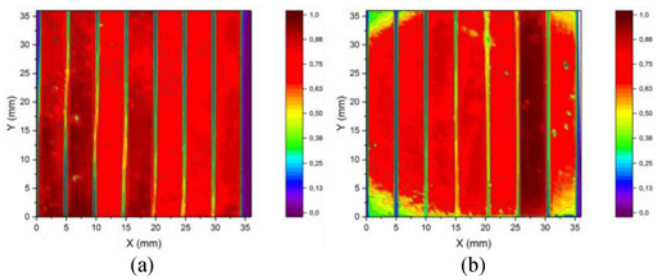

Fig. 6. LBIC map of a CsFAMA (a) and MALI (b) module.

perovskite. Indeed DEE, the antisolvent used in the MALI process, has a very high vapor pressure compared to the chlorobenzene used for CsFAMA modules. As a consequence, it might be less efficient in uniformly removing the excess DMF in the film upon spin-coating. Moreover, Saliba *et al.* [16] emphasized the higher robustness toward surrounding parameters such as temperature and solvent vapors of the CsFAMA perovskite over the MALI. Considering the larger area of the module substrates, these variations can become more critical in comparison to small cell substrates. In addition, toluene, a solvent with a vapor pressure comparable to that of chlorobenzene, has been used to produce MALI cells (see Supplementary information). However, the performance of these cells was significantly lower than using DEE. Therefore, the work on modules has been carried out with the latter.

Further work is currently ongoing to better identify the possible loss mechanisms between small-scale devices and modules as well as to further reduce the dead area. Additionally, ways of improving the stability of the devices are being investigated, mainly through the replacement of spiro-OMeTAD as a hole transport material. Finally, encapsulation schemes are being developed in order to withstand accelerated degradation testing.

IV. Conclusion

Laser patterning was successfully applied to two different PK layer compositions to realize the monolithic P1–P2–P3 module interconnections. Thanks to optimized scribing parameters, the dead area width between consecutive segments was greatly reduced down to 400 μm compared to previous work and similar contributions. This led to a minimal power loss when scaling up between single cells and modules. Finally, by careful choice of deposition parameters and device architecture, it was possible to demonstrate a record module with a steady-state efficiency of 16.0% on 14 cm^2 aperture area with a fraction of dead area as low as 8%.

References

[1] NREL, "NREL efficiency chart," Dec. 2, 2016. [Online]. Available: http://www.nrel.gov/pv/assets/images/efficiency_chart.jpg. Accessed on: Jan. 10, 2017.

[2] M. A. Green *et al.*, "Solar cell efficiency tables (version 49)," *Prog. Photovolt.*, vol. 25, no. 1, pp. 3–13, 2017.

[3] M. Cai *et al.*, "Cost-performance analysis of perovskite solar modules," *Adv. Sci.*, vol. 4, no. 1, 2017, Art. no. 1600269.

[4] W. S. Yang *et al.*, "High-performance photovoltaic perovskite layers fabricated through intramolecular exchange," *Science*, vol. 348, no. 6240, pp. 1234–1237, 2015.

[5] S. S. Shin *et al.*, "Colloidally prepared La-doped BaSnO3 electrodes for efficient, photostable perovskite solar cells," *Science*, vol. 356, no. 6334, pp. 167–171, 2017.

[6] F. Matteocci *et al.*, "Solid-state solar modules based on mesoscopic organometal halide perovskite: A route towards the up-scaling process," *Phys. Chem. Chem. Phys.*, vol. 16, no. 9, pp. 3918–3923, 2014.

[7] S. Razza *et al.*, "Perovskite solar cells and large area modules (100 cm2) based on an air flow-assisted PbI2 blade coating deposition process," *J. Power Sources*, vol. 277, pp. 286–291, 2015.

[8] R. Bartlome, B. Strahm, Y. Sinquin, A. Feltrin, and C. Ballif, "Laser applications in thin-film photovoltaics," *Appl. Phys. B*, vol. 100, no. 2, pp. 427–436, 2010.

[9] S.-J. Moon *et al.*, "Laser-scribing patterning for the production of organometallic halide perovskite solar modules," *IEEE J. Photovolt.*, vol. 5, no. 4, pp. 1087–1092, Jul. 2015.

[10] W. Qiu *et al.*, "An interdiffusion method for highly performing cesium/formamidinium double cation perovskites," *Adv. Funct. Mater.*, vol. 27, 2017, Art. no. 1700920.

[11] M. R. Leyden, Y. Jiang, and Y. Qi, "Chemical vapor deposition grown formamidinium perovskite solar modules with high steady state power and thermal stability," *J. Mater. Chem. A*, vol. 4, no. 34, pp. 13125–13132, 2016.

[12] A. Priyadarshi *et al.*, "A large area (70 cm2) monolithic perovskite solar module with a high efficiency and stability," *Energy Environ. Sci.*, vol. 9, no. 12, pp. 3687–3692, 2016.

[13] H. Booth, "Laser processing in industrial solar module manufacturing," *J. Laser Micro/Nanoeng.*, vol. 5, no. 3, pp. 183–191, 2010.

[14] J. Hüpkes, J. Müller, and B. Rech, "Texture Etched ZnO:Al for silicon thin film solar cells," in *Transparent Conductive Zinc Oxide*. Berlin, Germany: Springer, 2008, pp. 359–413.

[15] N. Ahn *et al.*, "Highly reproducible perovskite solar cells with average efficiency of 18.3% and best efficiency of 19.7% fabricated via Lewis base adduct of lead(II) iodide," *J. Amer. Chem. Soc.*, vol. 137, no. 27, pp. 8696–8699, 2015.

[16] M. Saliba *et al.*, "Cesium-containing triple cation perovskite solar cells: Improved stability, reproducibility and high efficiency," *Energy Environ. Sci.*, vol. 9, no. 6, pp. 1989–1997, 2016.

[17] L. Bayer, X. Ye, P. Lorenz, and K. Zimmer, "Studies on perovskite film ablation and scribing with ns-, ps- and fs-laser pulses," *Appl. Phys. A*, vol. 123, no. 10, 2017, Art. no. 619.

[18] W. Qiu *et al.*, "Pinhole-free perovskite films for efficient solar modules," *Energy Environ. Sci.*, vol. 9, no. 2, pp. 484–489, 2016.

[19] F. Matteocci *et al.*, "High efficiency photovoltaic module based on mesoscopic organometal halide perovskite," *Prog. Photovolt., Res. Appl.*, vol. 24, no. 4, pp. 436–445, 2016.

Authors' photographs and biographies not available at the time of publication.